Noname manuscript No.
(will be inserted by the editor)

Wave patterns generated by an axisymmetric obstacle in a two-layer flow.

Laurent Lacaze · Alexandre Paci · Emmanuel Cid · Sébastien Cazin · Olivier Eiff · JG Esler · ER Johnson

Received: date / Accepted: date

Abstract **Keywords** First keyword · Second keyword · More

1 Introduction

Flow interaction with an immersed obstacle can lead to surface waves but also to internal gravity waves if the fluid is density stratified. The case of an obstacle on the horizontal boundary of the flow is particularly interesting as it is a configuration similar to topographically-generated internal gravity waves in geophysical flows. These waves are in particular studied for their role on mixing and global circulation in the ocean [21,24] and on momentum transport and drag in the atmosphere [25,26]. When the vertical stratification is such that internal gravity waves energy is trapped and cannot propagate vertically, as at the bottom of the oceanic mixed layer [3,22] or at the top of the atmospheric boundary layer [23,12], waves can be studied as interfacial waves between two layers of fluid. Camassan and Tiron [6] show that under certain condition a two-layer model can be used to provide quantitative information on internal gravity waves propagating in a more general vertical stratification. Some recent laboratory experiments have focused on such waves in a two layer flow, but they lack instantaneous 3D interface elevation measurements, the interface height being retrieved either from local probes [17,20] or from a vertical plane intersecting the interface [18].

In the present study, an optical stereoscopic technique is deployed to measure an instantaneous field of the elevation of an interface located between two layer of fluid. Stereoscopic techniques have been widely used to measure surface elevation in free surface flows [4,7,9, 10,14]. The technique is based on the determination of the position of different points, in the laboratory frame of reference, via their imaged positions in the image planes of two separate cameras. The three-dimensional position of these points at different times thus yields quantitative information on the evolution of the free surface. However tracking an interface is less straightforward as particles are spread vertically over the non-zero interface thickness.

The main part of the algorithm used here was previously developed for the quantification of the sand bed evolution in the swash zone of a beach in a large-scale lab experiment [1]. In this previous study, dots aligned on a regular grid were projected on the beach. The center of the image dots on each camera plane were thus easily extracted and matched for 3D reconstruction. Here, the algorithm is extended to the case of random patterns using a cross-correlation technique in order to measure an interface randomly seeded with particles. This method give access, for the first time, to the full wave field induced by an obstacle towed on top of the upper layer of two layer of comparable depth in a large-scale lab experiment (Fig. 1). These experiments were inspired by recent theoretical works [16,17,

L. Lacaze · E. Cid · S. Cazin · O. Eiff
Université de Toulouse; INPT, UPS; IMFT(Institut de Mécanique des Fluides de Toulouse); Allée Camille Soula, F-31400 Toulouse, France
CNRS; IMFT; F-31400 Toulouse, France
E-mail: laurent.lacaze@imft.fr

A. Paci
URA1357 Météo-France and CNRS; CNRM-GAME/GMEI/SPEA; 42 av. G. Coriolis; 31057 Toulouse Cedex 1, France
E-mail: alexandre.paci@meteo.fr

JG Esler · ER Johnson
Department of Mathematics, University College London, 25 Gower Street, London WC1E 6BT, UK

11] predicting the wave structure in similar flows where dispersive effects dominate over dissipative effects, as in many geophysical situations. Under certain conditions, for example when the flow speed is close to the gravity waves speed, these results lead to different predictions than previous work in the non-dispersive limit (e.g. [27, 15]).

In section 2, the experimental set-up is presented, in particular a detailed description of the measurement technique and the associated validation. Section 3 is devoted to the gravity waves analysis. Finally, a discussion on the obtained results is proposed is section 4.

2 Experimental procedure

2.1 Experimental set-up

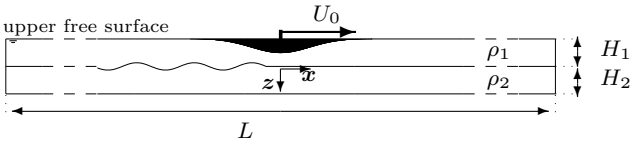

Fig. 1 Sketch of the experimental set-up ($L = 22$ m and $H_1 \approx H_2 \approx 15$ cm).

The experiments are performed in the large stratified water flume at the geophysical fluid mechanics laboratory of CNRM-GAME in Toulouse. The flume is used here as a 22 m long, 3 m wide and 1 m high towing tank. The tank is filled with a stratified two-layer fluid made of saline water with two different concentrations of salt. The two saline layers are characterised by their respective height H_i and density ρ_i, $i = 1$ corresponding to the layer in which the obstacle is immersed and $i = 2$ the other layer (top and bottom layers in Fig. 1, respectively). Typical values are $H_1 \approx 15$ cm, $\rho_1 = 1000$ kg.m^{-3}, $H_2 \approx H_1$ or (slightly) larger and $\rho_2 = 1059$ kg.m^{-3}. As those quantities evolve somewhat in time, they are systematically measured before each experiment. The total height $H = H_1 + H_2$ is fixed. All the experiments described in the following correspond to an interface thickness of no more than a few centimetres. A typical density profile $\rho(z)$, obtained with a conductivity probe, is shown in figure 2. In order to extract the vertical position and the thickness of the interface, the raw data are fitted with the function

$$\rho = \frac{\rho_2 - \rho_1}{2} \tanh\left(\frac{z - h_i^f}{e^f}\right) + \frac{\rho_2 + \rho_1}{2}, \qquad (1)$$

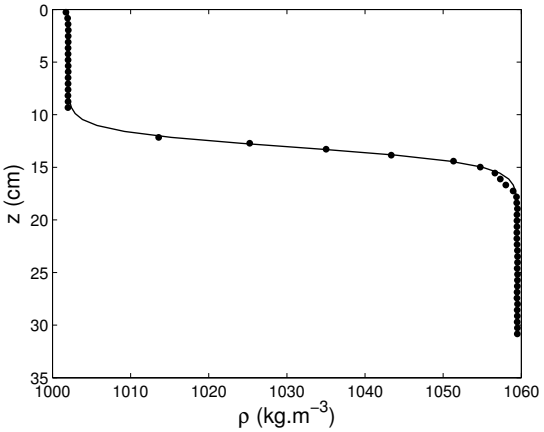

Fig. 2 Density variation ρ along the vertical axis z. Dot symbols correspond to the experimental measurements and the solid line is the best fit estimated accordingly to equation (1) with $\rho_1 = 1000$ kg.m^{-3}, $\rho_2 = 1059$ kg.m^{-3}, $e^f = 1.35$ cm and $h_i^f = 12.84$ cm.

where superscript f denotes a fitting parameter and with h_i and e the vertical position and thickness of the interface respectively. Fitting parameters are then used to estimate the non-dimensional numbers of each experiments presented below. The density ρ_i of each layer is obtained from direct measurements using an accurate densitometer. Superscripts f are omitted in the following.

Two axisymmetric obstacles, referred as A and B in the following, of base diameter 100 cm and maximum heights $h_m^0 = 7.7$ cm and $h_m^0 = 12.5$ cm respectively, are towed in the tank at velocity U_0 (see Fig. 1). Their radial profile is such that $h_m(r) = h_m^0 \exp(-2r^2/l^2)$ with $l = 32$ cm. The obstacles are towed upside down in the top layer (see Fig. 1) to avoid interfering wires and supports with the interface. Therefore, the $\boldsymbol{z}$ axis points downward and $z = 0$ is set at the upper free surface. The $\boldsymbol{x}$ axis is aligned with the towing direction of the obstacle. In the following, the results are shown in the frame moving with the obstacle, $x = 0$ being at the centre of the obstacle.

In this experimental configuration, three non-dimensional numbers are traditionally defined: the Froude number $Fr = U_0/c$; the non-dimensional obstacle height $M = h_m^0/H_1$[1] and the aspect ratio $\delta = H_1/l$, where $c = (g' H_1 H_2/(H_1 + H_2))^{1/2}$ is the phase velocity of the gravity wave evolving at the interface; $g' = 2g(\rho_2 - \rho_1)/(\rho_2 + \rho_1)$ is the reduced gravity. A fourth parameter, $\Gamma = (Fr - 1)M^{-2/3}$, emerges from a previous study in the case of a single layer flow [11] and is known as the transcritical similarity parameter. The range of parameters

[1] As obstacles are towed upside-down, they cannot be fully immersed, so effective h_m^0 is slightly smaller than the values given above and is 7.5 cm (resp. 11.5 cm) for A (resp. B).

Table 1 Range of experimental parameters for A (1st row) and B (2nd row)

	Fr	M	δ	Γ
A	$0.24, 1.44$	$0.49, 0.59$	$0.48, 0.40$	$-1.22, 0.63$
B	$0.49, 1.48$	$0.90, 1.60$	$0.41, 0.22$	$-0.55, 0.55$

of the different experiments performed here is given in Table 1 for A and B.

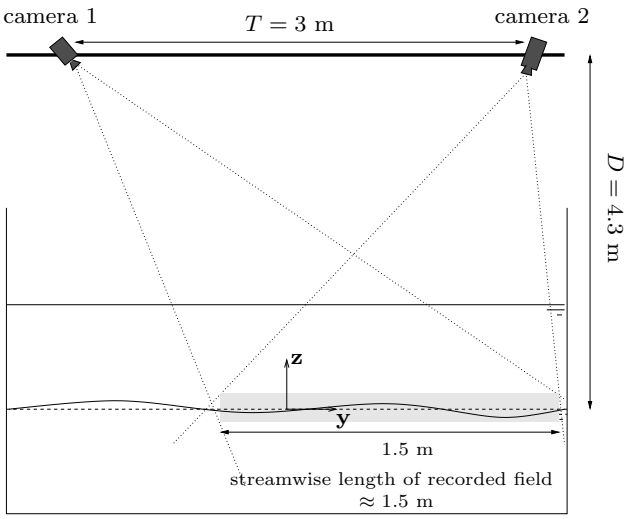

(frontal view)

Fig. 3 Sketch of the stereovision system set-up (not to scale) in the frontal (y, z) plane. The two cameras image the interface of the two-layer fluid over 1.5×1.5 m^2. Dotted lines delineate the filed of view of each camera. The horizontal dash line correspond to position of the interface at rest. The frontal projection of the measurement volume is represented by the grey area.

In the present study, the stereo system was chosen to be fixed in the laboratory frame so that large x ($\gg 1.5$ m) can be observed. The measured zone is a 1.5 m $\times$ 1.5 m horizontal field. In the vertical direction, the deformation of the interface is of the order of few centimeters. Two synchronised high-resolution, high-sensitivity 14-bit PCO-2000 cameras (2048×2048 pix^2 with a CCD cell size of 7.4×7.4 μm^2) were chosen, coupled to 35 mm Nikon Nikkor lenses ($f = 35$ mm). The cameras were attached on a rigid and strong steel and aluminium structure, the distance between the cameras and from the zone of interest being about $T \sim 3$ m and $D \sim 4.3$ m, respectively (see Fig. 3). The two cameras thus recorded the same field, at 2 Hz, with an angle between the two line of sights of around 40°.

2.2 Stereo system

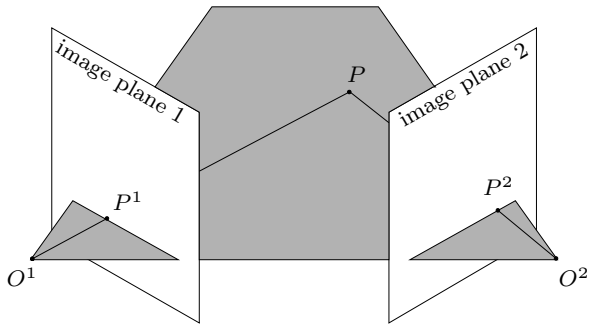

Fig. 4 Binocular stereovision configuration. The two image points P^1 and P^2 of the point P are located on the line of sight of each camera.

The stereoscopic method can be summarized as follows. If one considers a point P in the laboratory frame of reference (i.e. the world coordinates) imaged by two cameras, here referred to as cameras 1 and 2 (fixed in the laboratory frame of reference and not aligned), the process to determine its position $P_{|w} = (x_w, y_w, z_w)$ in the world coordinate frame of reference is known as triangulation. Triangulation is the identification of the intersecting point between the two different lines of sight –rays– passing through the two image points of P, P^1 and P^2 and with O^1 and O^2 the centres of the optical systems associated with cameras 1 and 2, respectively (see Fig. 4). This procedure gives access to the third spatial dimension, lost by imaging a scene with only one camera, by using the information from both cameras.

The stereo camera model as well as the calibration process used in the present study is similar to the one presented in Astruc *et al.* [1]. It will thus not be detailed here and the reader is referred to Astruc *et al.* [1] for details. However, the specific experimental set-up of the stereo system used in the experiment and the stereo matched technique needed some modification to extend the method to the case of a random seeded scene. In particular, a stereo-matching algorithm adapted to random pattern has been developed. As our scene exhibits different slopes, this implies that the images of a same pattern, acquired by left and right cameras, are often very different. This leads to failure of the matching process considering simple cross-correlation operation between images from left end right cameras. So, in order to improve reliability, our matching process is done in two steps. First, from the previous calibration, homography

matrix is calculated to transpose the left and right images in a common plane [13]. The images are processed by epipolar rectification. Therefore, the mapping operation is reduced to a 1D search along the x-axis on each image. We then applied a growing correspondence seeds algorithm [5]. This previous mapping serves as a predictor and allows us to locally deform raw images in order to increase their similarity. The matching is then refined by cross-correlation with interrogation window size of 32×32 pix^2. The cross-correlation, with image deformation, is applied twice using 'cubic spline' image interpolation scheme. Finally, the obtained 3D reconstruction is adjusted to take into account the change of refractive index through the upper free-surface crossed by the line of sights of both cameras.

A validation of the method is performed using A cov-

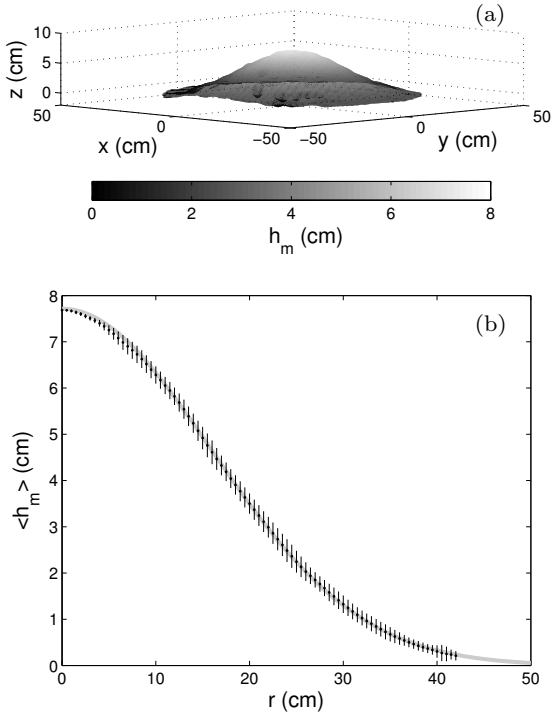

Fig. 5 3D reconstruction of the obstacle shape using the optical stereoscopic method: (a) contour of the obstacle in the world coordinate system, (b) averaged radial profile $< h_m >$ (dots) and the associated standard deviation (vertical solid lines). (Gray solid line corresponds to the best fit as explained in the text.)

ered with random white dot patterns, which is placed up side up on the bottom of a water layer of thickness $H = 30$ cm, to take into account the presence of the free-surface. The 3D reconstruction of the surface h_m is shown in Fig. 5(a). The accuracy of the method can then be estimated by comparing the averaged surface profile $< h_m > (r)$ with the theoretical profile $h_m^0 \exp(-2r^2/l^2)$, r being the radial coordinate centred at the summit of the obstacle and $< . >$ denoting the azimuthal averaging. The result is shown in Fig. 5(b) in which dots correspond to the mean profile $< h_m > (r)$. The error of the measured profile is estimated as being twice the standard deviation along the azimuthal direction and is shown in Fig. 5(b). The obtained experimental profile is fitted with a function of the type $h_e \exp(-2r^2/l_e^2)$ with $h_e = 7.716$ cm and $l_e = 31.65$ cm (gray line in Fig. 5(b)). The error given by the two fit parameters is therefore of the order of 500 μm while the error associated with the standard deviation gives a maximum error of 3 mm at the maximum slope of the obstacle. It has to be noted that the latter error slightly overestimates the error induced by the stereo method since it includes the accuracy of the manufactured shape, of the order of 1 mm. The obtained accuracy of the method is therefore well below the measured interface displacement which is of the order of few centimetres as shown in the following.

3 Gravity-wave pattern analysis

3.1 Stationary wave field

Figures 6(a,b,c,d) show the interface height anomaly η in the laboratory frame of reference (X, Y) obtained at four different times t, with an interval of 10 frames, *i.e.* 5 s, between images (a), (b), (c) and (d)[2]. The next step of the experimental data analysis is the reconstruction of the interface height field in the frame of reference of the moving obstacle (x, y). As the velocity U_0 of the towed obstacle is constant and waves are steady in the frame, the reconstruction only consists in shifting each measured field in the horizontal direction of propagation, *i.e.* $x = X - U_0 t$, without any phase alignment between the different $\eta(X, Y, t)$ fields. To this end, the sampling rate (2 Hz) has been chosen in order to ensure a spatial overlap of successive images in the obstacle frame of reference. The reconstruction resulting from Figures 6(a,b,c,d) is shown in figure 6(e). A stationary wake (in the frame moving with the obstacle) is therefore obtained. There is some wave reflection from the side walls of the flume ($y = 150$ cm) but this does not influence quantitative information extracted from the data. The latter point is discussed in the final section.

[2] $t = 0$ is defined here for the frame in which the obstacle centre coincides with the centre of the field of view.

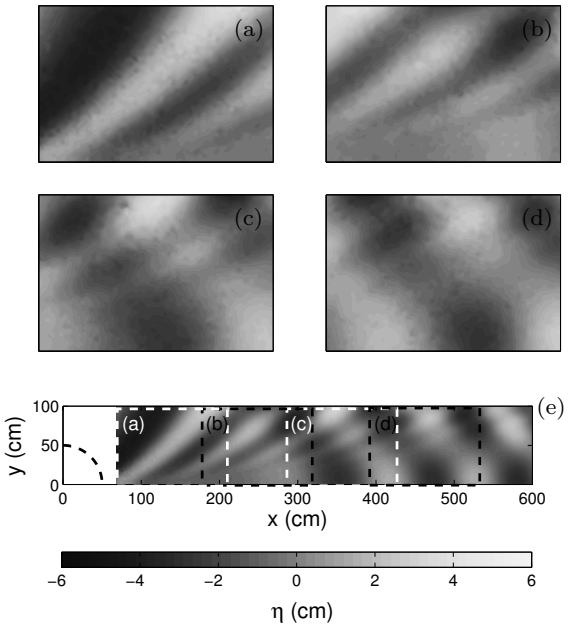

Fig. 6 Reconstruction of the stationary wave pattern in the frame of the obstacle for $Fr = 0.98$, $M = 0.87$ ($\Gamma = -0.02$).

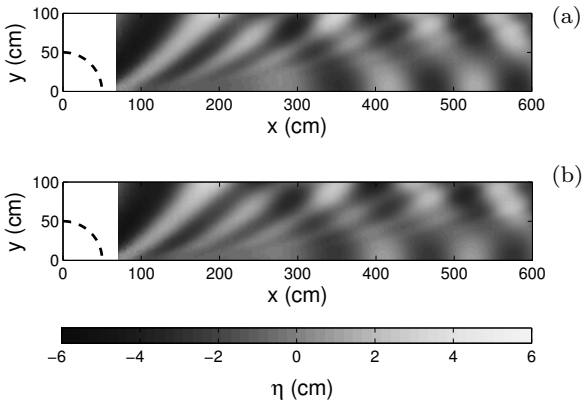

Fig. 7 Wave pattern for $Fr = 0.98$, $M \approx 0.95$ ($\Gamma = -0.02$); $e/H_1 = 0.2$ (a) and $e/H_1 = 0.3$ (b)

As the interface thickness e evolves between experiments, it is important to evaluate its influence on the gravity wave characteristics. To this end, two experiments correspondind to different values of e are compared, the other parameters being similar between the two experiments (see figure 7). For these two specific experiments, the parameters are $Fr = 0.98$, $M \approx 0.95$ (0.92 and 0.96 respectively) and $e/H_1 = 0.2$, 0.3 respectively. As observed in figures 7(a) and 7(b), the evolution of e/H_1 is not significant enough to induce a modification of the wave pattern.

Moreover the parameter δ, which characterizes the dispersion due to non-hydrostatic effects, lies in a narrow range of moderate dispersion. Its influence on the following analysis is therefore considered as negligible.

3.2 Wake analysis

Typical examples of gravity wave patterns obtained for different experimental parameters are shown in Fig. 8. Wave patterns generated by A (resp. B) are shown in the left hand-side column (resp. right hand-side column). Each column corresponds to a given value of M: $M = 0.6$ for A and $M = 0.9$ for B. Moreover, for each obstacle, the amplitude range of η displayed is fixed in order to compare the relative wave deformation generated for different parameters. The influence of the Fr on the wave pattern is clearly highlighted through a modification of the wave structures. In particular, waves patterns in Figs. 8(a) and 8(b) with $Fr < 0.7$ are representatives of subcritical flows while Figs. 8(c) and 8(d) although $Fr \lesssim 1$, and even more clearly Figs. 8(e) and 8(f) where $Fr > 1$, show features characterized by supercritical flows with in particular a well defined Mach angle.

The energy that is injected in the wave field is quantified by the potential energy associated to the interface displacement. In the following, one defines the non-dimensional potential energy as

$$E_p = \frac{1}{\rho_m g H} \max_{\mathcal{D}(x_m)} \frac{1}{S_{\mathcal{D}(x_m)}} \int_{\mathcal{D}(x_m)} \frac{1}{2}(\rho_2 - \rho_1) g \eta^2 dS, \tag{2}$$

where $\rho_m = (\rho_1 + \rho_2)/2$ is the mean density and $\mathcal{D}(x_m)$ is the horizontal area defined as $x < x_m$. A variable domain from case to case, x_m being the streamwise position leading to a maximum of E_p, is preferred to a fixed domain since the significant spatial region of variation of the potential energy can depend on the regime considered, from subcritical to supercritical.[3] The potential energy E_p as a function of Fr for the two obstacles is shown in Figs. 9(a) and 9(b) for A and B respectively. Inlets in Figs. 9(a) and 9(b) show for information E_p as a function of Γ. Fig. 9 highlights the increase of energy transferred to gravity waves around the critical regime $Fr = 1$ or equivalently $\Gamma = 0$, as it is found in the case of a single layer flow from the consideration of the wave drag [11]. Moreover, there exists a range of Γ for which the value of the potential energy is significantly increased which can be associated with the transcritical

[3] It is verified that the obtained value of x_m is always smaller than the distance at which reflective waves invade the domain.

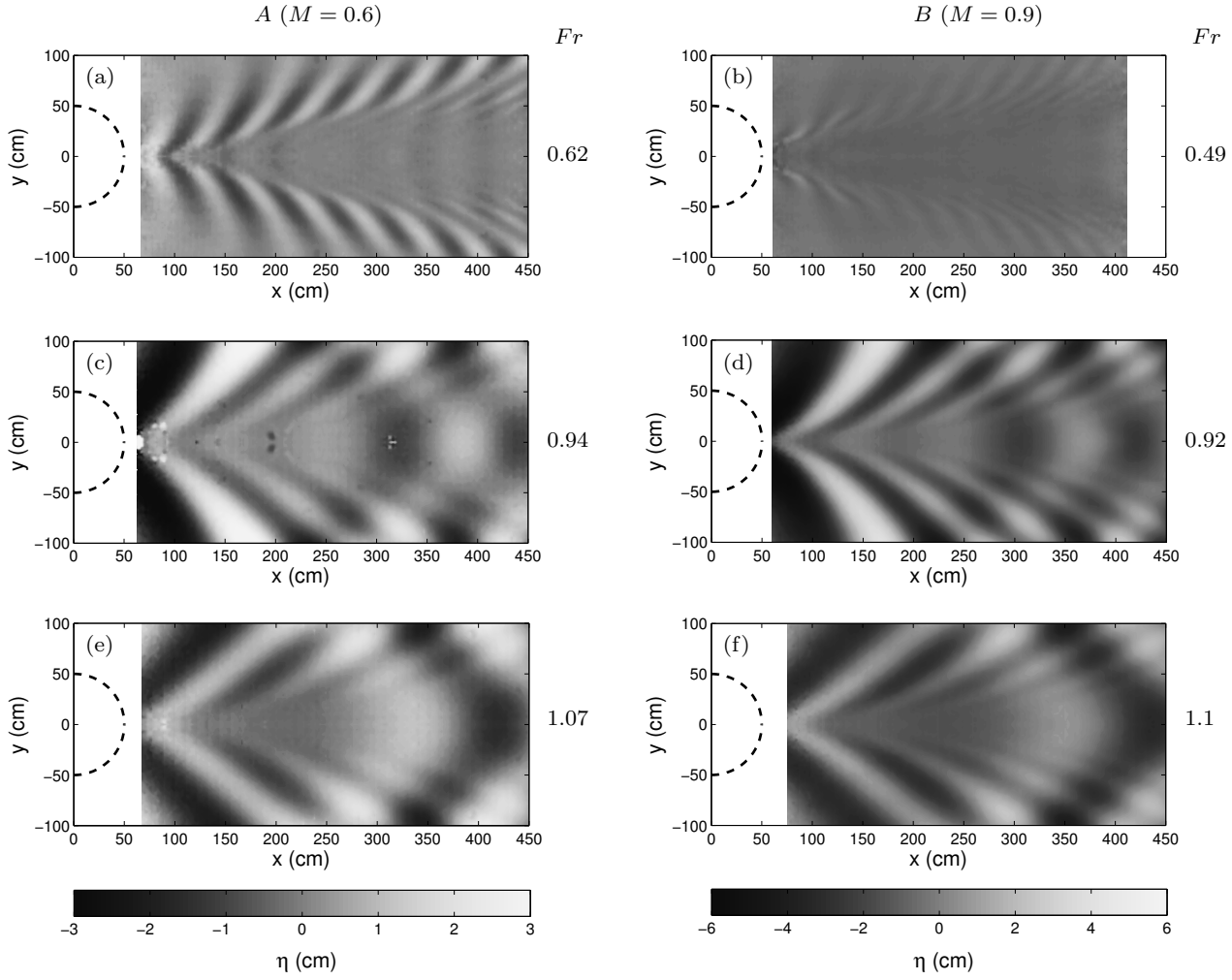

Fig. 8 Different gravity-wave patterns for A (left column), $M = 0.6$, and B (right-hand side column), $M = 0.9$; (a) $Fr = 0.62$, (b) $Fr = 0.49$, (c) $Fr = 0.94$, (d) $Fr = 0.92$, (e) $Fr = 1.07$ and (f) $Fr = 1.1$ ($\Gamma = [-0.55, -0.08, 0.1]$ from top to bottom).

regime. This specific regime delimited by the subcritical regime and supercritical regime has been mostly studied in the case of single layer flows [11]. In the set of experiments considered here, it it is difficult to quantitatively delineate the different regimes. Nevertheless, top row of Fig 8, $Fr < 0.7$ and $\Gamma = -0.53$, is clearly typical of a subcritical regime for which a wave packet defined by a wave vector oriented with a given angle from the direction of the flow is observed. On the other hand, bottom row of Fig 8 shows the wake structure of a supercritical flow characterized by an oblique shock wave and a Mach angle.

4 Discussion

Based on previous theoretical results in which the influence of Γ on the wake dynamics were highlighted [11], the experimental results can be characterized by the parameter Γ instead of Fr. For instance, wave patterns in Fig 8 are such that $\Gamma = [-0.53, -0.08, 0.1]$ from top to bottom and independent of the considered obstacle (i.e. from one column to the other). Even if a difference in the relative amplitude between $M = 0.6$ and $M = 0.9$ for $\Gamma = -0.53$ is observed, and probably attributed to the difference in Fr between these two experiments, the non-dimensional number Γ shows to be pertinent to characterize the spatial structure of the wave patterns in the configuration studied here. Following this feature,

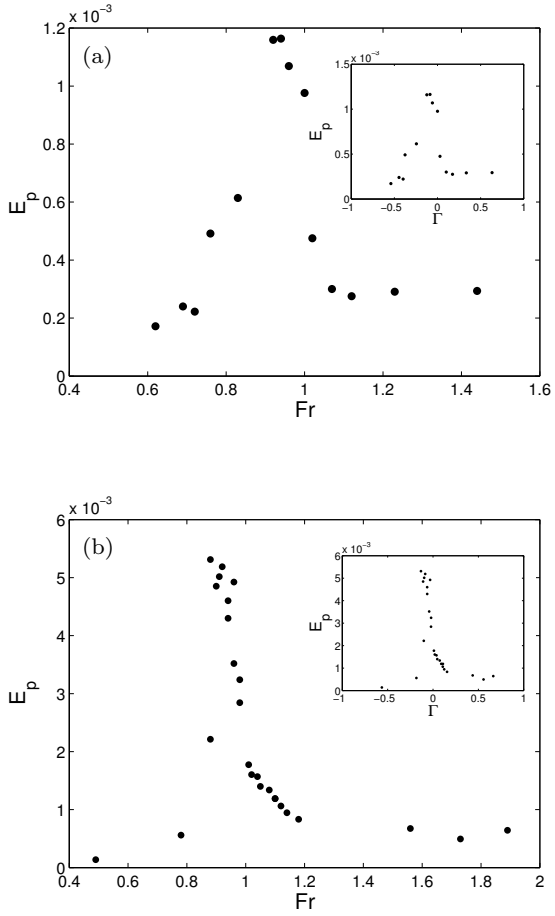

Fig. 9 Potential energy E_p as a function of Fr for (a) A and (b) B. Inlets present results as a function of Γ.

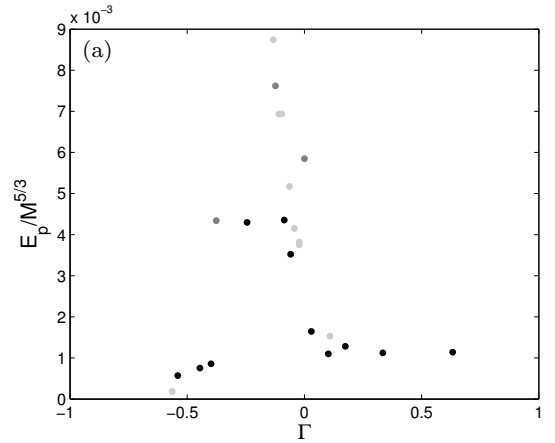

Fig. 10 Potential energy as a function of Γ for different ranges of M; $0.5 < M < 0.55$ (black dots) and $0.55 < M < 0.6$ (dark gray dots) for A and $0.85 < M < 0.95$ (light gray dots) for B.

a normalized potential energy is derived following the theoretical analysis of Esler *et al.*[11] in order to rescale the two set of experiments. In particular, $E_p/M^{5/3}$ is shown as a function of Γ in figure 10. In the case of single layer flows, this normalization emerges from a similarity theory developed for transcritical flow. The nondimensional drag is therefore shown to take the form $D(\Gamma)M^{5/3}$. However, it was found that if M becomes too large (typically around 0.5) the flow characteristics slightly diverge from the theory. In order to take into account this large M effect that might be of importance in the present configuration ($M > 0.5$ in all the experiments), the data in figure 10 has been distinguished such as $0.5 < M < 0.55$ (black dot), $0.55 < M < 0.6$ (dark gray dots) and $0.6 < M < 0.95$ (light gray dots). Even if a clear tendency does not emerge from the different M intervals, Fig. 10 highlights the pertinence of the normalization used for single layer flows and extended here to a two-layer flows. In particular, the different gray symbols seem to define peaked curves whose maxima occur at the same value of $\Gamma \sim -0.15$.

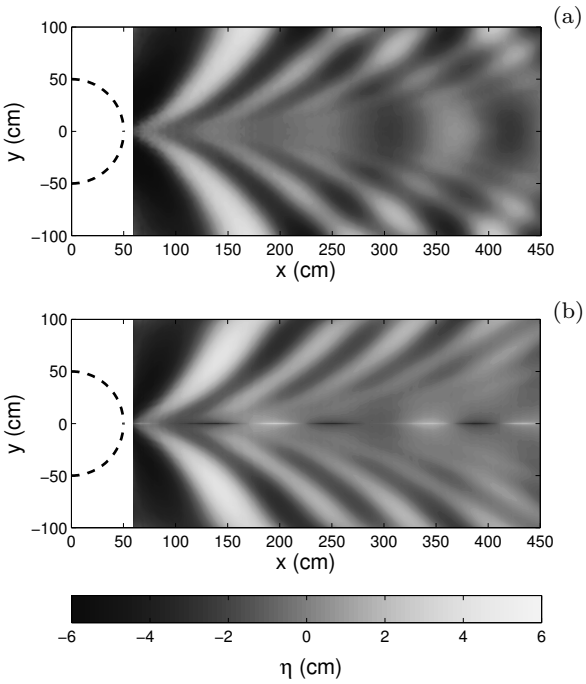

Fig. 11 Wave pattern for $\Gamma = -0.08$, $M \sim 0.9$: raw data (a) and filtered data (b).

The experimental study presented in this paper shows the gravity wave patterns generated in the wake of an axisymmetric obstacle. Due to the geometry of the system considered here, waves are reflected on the side

wall of the flume and invade the field of measurement at some distance of the obstacle (as observed in Fig. 8). This behaviour is more significant in the transcritical regime characterised by waves propagating nearly perpendicular to the streamwise direction. A first attempt to eliminate reflected waves is presented here using a Hilbert transform filter as explained in Mercier *et al.*[19]. Results are shown in Fig. 11 for the case $\Gamma = -0.08$ and $M = 0.9$, *i.e.* in the transcritical regime (raw pattern (a) and filtered pattern (b)). Even if disturbances appear on the axis of symmetry, the obtained filtered pattern is qualitatively convincing. Nevertheless, the potential energy calculated here and presented in the previous section was preferred to be calculated with the non-filtered results, the reason being that gravity waves are strongly non-linear in the present case while the filtering method is based on a linear approach. However, the spatial domain containing the maximum energy is found to be not influenced by the reflective waves, *i.e.* x_m is always below 200 cm.

5 Conclusion

Bi-dimensional gravity wave patterns forced by an obstacle in a two-layer fluid have been experimentally studied. In particular, attention has been paid on the influence of the Froude number Fr and the non-dimensional height M, or equivalently the transcritical similarity parameter Γ. General features associated to subcritical and supercritical fluid flows have been highlighted. It is moreover shown that close to the critical point, a transcritical regime is characterized by a rapid evolution of the potential energy stored in the gravity waves. Moreover, in accordance to the case of a single layer, the normalization $E_p/M^{5/3}$ is shown to be pertinent to merge the different experimental results as a function of the parameter Γ.

Acknowledgements The experiments described in this publication were supported by the European Community's Sixth Framework Programme through the grant to the budget of the Integrating Activity HYDRALAB III, Contract no. 022441(RII3). This document reflects only the authors' views and not those of the European Community. This work may rely on data from sources external to the HYDRALAB III project Consortium. Members of the Consortium do not accept liability for loss or damage suffered by any third party as a result of errors or inaccuracies in such data. The information in this document is provided "as is" and no guarantee or warranty is given that the information is fit for any particular purpose. The user thereof uses the information at its sole risk and neither the European Community nor any member of the HYDRALAB III Consortium is liable for any use that may be made of the information. We thank A. Belleudy, B. Beaudoin, B. Bourdelles, J.-C. Boulay, J.-C. Canonici, F. Murguet, M. Morera, S. Lassus Pigat and H. Schaffner of the CNRM-GAME geophysical fluid mechanics laboratory in Toulouse for their kind support . We thank also Joseph Pearce and Orial Kryeziu for their participation in these experiments.

References

1. Astruc D., Cazin S., Cid E., Eiff O., Lacaze L., Robin P., Toublanc F., Cáceres I. (2012) A stereoscopic method for rapid monitoring of the spatio-temporal evolution of the sand-bed elevation in the swash zone. Coastal Eng., **60**:1–20.
2. Baines PG, Topographic Effects in Stratified Flows. Cambridge University Press (1995)
3. Apel J, Holbrook J, Liu A, Tsai J (1985). The sulu sea internal soliton experiment. Journal of Physical Oceanography. **15**(12): 1625-1651.
4. Benetazzo A (2006) Measurements of short water waves using stereo matched image sequences. Coast. Eng. **53**:1013.
5. Cech J, Sara R (2007) Efficient Sampling of Disparity Space for Fast and Accurate Matching, in: Proc. BenCOS Workshop CVPR.
6. Camassa R, Tiron R (2011) Optimal two-layer approximation for continuous density stratification. J. Fluid Mech. **669**:32-54.
7. Chatellier L, Jarny S, Gibouin F, David, L (2010) Stereoscopic measurement of free surface flows., in: 14th International Conference on Experimental Mechanics, Poitiers, France.
8. Choi W, Camassa R (1999) Fully nonlinear internal waves in a two-fluid system. J. Fluid Mech. **396**:1.
9. de Vries S, Hill DF, de Schipper MA, Stive MJF (2011) Remote sensing of surf zone waves using stereo imaging. Coast. Eng. **58**:239.
10. Douxchamps D, Devriendt D, Capart H, Craeye C., Macq B, Zech Y (2005) Stereoscopic and velocimetric reconstructions of the free surface topography of antidune flows. Exp. Fluids **39**:533.
11. Esler JG, Rump OJ, Johnson ER (2007) Non-dispersive and weakly dispersive single-layer flow over an axisymmetric obstacle: the equivalent aerofoil formulation. J. Fluid Mech. **574**:209.
12. Goler RA, Reeder MJ (2004). The Generation of the Morning Glory. J. Atmos. Sci. **61**: 13601376.
13. Hartley RI, Zisserman A, Multiple View Geometry in Computer Vision, Cambridge University Press (2004)
14. Jehle M, Jarny S, David L (2008) Différentes approches pour la mesure d'interfaces et de surface libre, in: 11ème Congrès Francophone de Techniques Lasers, Poitiers, France. pp. 225. (In French)
15. Jiang Q, Smith RB (2000) V-waves, blow shocks, and wakes in supercritical hydrostatic flow. J. Fluid Mech. **406**:27.
16. Johnson ER, Vilenski GG (2005) Two-dimensional leaps in near-critical flow over isolated orography. Proc. R. Soc. Lond. A **61**(2064):3747-3763.
17. Johnson ER, Esler JG, Rump OJ, Sommeria J, Vilenski GG (2006) Orographically generated nonlinear waves in rotating and non-rotating two-layer flow . Proc. R. Soc. Lond. A **462**(2065):3-20.
18. Knigge C, Etling D, Paci A, Eiff O (2010) Laboratory experiments on mountain induced rotors. Quarterly Journal Royal Meteorological Society **136**: 442-450.

19. Mercier MJ, Garnier NB, Dauxois T (2008) Reflexion and diffraction of internal waves analyzed with the Hilbert transform. Phys. Fluids **20**:086601.
20. Mercier MJ, Mathur M, Gostiaux L, Gerkema T, Magalhes JM, Da Silva JCB, Dauxois T (2012) Soliton generation by internal tidal beams impinging on a pycnocline: laboratory experiments. J. Fluid Mech. **704**:37-60.
21. Munk W, Wunsch C (1998) Abyssal recipes II : energetics of tidal and wind mixing Deep Sea Research Part I : Oceanographic Research Papers **45**(12): 1977-2010.
22. New A L, Pingree RD (1992) Local generation of internal soliton packets in the central bay of biscay. Deep Sea Research Part A. Oceanographic Research Papers, **39**(9): 1521-1534.
23. Porter A., Smyth NF (2002). Modelling the morning glory of the Gulf of Carpentaria. J. Fluid Mech., **454**: 1-20.
24. Tailleux R. (2009) On the energetics of stratied turbulent mixing, irreversible thermodynamics, boussinesq models and the ocean heat engine controversy. Journal of Fluid Mechanics, **638**: 339-382.
25. Smith RB (1979) The influence of mountains on the atmosphere. Adv. Geophys. **33**:87-230.
26. Wells H, Vosper SB (2010) The accuracy of linear theory for predicting mountain-wave drag: Implications for parametrization schemes. Q. J. R. Meteorol. Soc. **136**: 429441.
27. Schar C., Smith R.B. (1993) Shallow-water flow past an isolated topography. Part I: Vorticity production and wake formation. J. Atmos. Sci. **50**: 13731400.